Desalination and Water Treatment
www.deswater.com

doi: 10.5004/dwt.2022.28021

246 (2022) 68–81
January

Effects of forced input on the performance of direct contact membrane distillation

Emad Ali[a,*], Jamel Orfi[b], Abdullah Najib[b]

[a]*Chemical Engineering Department, King Saud University, Riyadh, Saudi Arabia 11421, Tel. +966114676871; email: amkamal@ksu.edu.sa (E. Ali)*
[b]*Mechanical Engineering Department, King Saud University, Riyadh, Saudi Arabia 11421, emails: orfij@ksu.edu.sa (J. Orfi), anmohammed@ksu.edu.sa (A. Najib)*

Received 6 September 2021; Accepted 30 November 2021

ABSTRACT

The effect of the input dynamics on the membrane distillation performance is studied employing an experimentally validated model. Alteration of the cold stream flow rate relative to the hot stream flow rate demonstrated a profound impact on the process dynamics, hydrodynamics, and heat-transfer mechanism. The process exhibited a variable dynamic response to fluctuation in feed temperature and flow rate. For example, the fundamental time constant can be from 0.3 min for step changes in the feed flow rate orating at feed temperature of 50°C to 18 min for step changes in the feed temperature operating at a flow rate of 500 L/h. Forcing both flow rates as opposite rectangular waves indicated enhancement of the accumulated gain output ratio (GOR) and the recovery ratio (RR). On an accumulative basis, GOR can improve by 60% and RR by 80%. Furthermore, decreasing the cycling frequencies of both flow rates can further improve the performance. Maximum performance enhancement was achieved when an equal period of oscillation of 5 min is utilized for both streams where GOR approaches 1 and RR 16%.

Keywords: Water desalination; Membrane distillation; Input forcing; Performance; Periodic operation

1. Introduction

Water and energy are currently the most vital commodities for human life. The demand for these resources increases exponentially because of the rapid increase and expansion of population and industrialization. The global demand for portable water was ~4 × 10^9 m^3 in the year 2000, and it is expected to grow by 58% in the year 2030 [1]. This growing demand requires a projected expansion of the desalination capacity. However, all the currently employed and projected desalination technologies, namely the multistage flash (MSF), multiple-effect distillation (MED), and reverse osmosis (RO), are energy-intensive methods. Hence, the expected expansion of the water desalination technology will impose additional constraints on the energy consumption and environmental impacts associated with brine discharge. It is expected that the energy consumption due to planned desalination projects will grow to 2.4 GWh by 2030 [1]. Therefore, to maintain future sustainability, more energy-efficient desalination techniques must be pursued. Recently, membrane distillation (MD) technology emerged as a promising alternative because of its various attractive features including being powered by low-grade energy sources [2–6]. Studies demonstrated MD ability to treat high salinity solutions [2,6]. MD combines thermal and membrane technologies for the separation of pure water from a saline solution. Direct contact MD (DCMD) is a generation of MD that has recently attracted significant

* Corresponding author.

1944-3994/1944-3986 © 2022 Desalination Publications. All rights reserved.

research interest and is implemented in multipurpose applications [3,7,8]. It is believed to afford a high gain output ratio (GOR), compared to other MD configurations, if effectively tuned [9]. Despite the appealing characteristics of the MD process in general, the widespread commercialization of MD is still limited because of some limitations. Mainly fouling, membrane wetting, and low recovery ratio (R_c) have been identified as main shortcomings [2–4,10–12]. Nevertheless, small-scale MD plants, for water production, are being set up in several locations [3,13]. Despite the recent commercialization of low-capacity MD systems, further investigations are necessary to promote its widespread and large-scale applications [5,13].

Resultantly, the literature is flooded with diverse investigations covering different aspects of the MD technology to address its limitations and promote it as an inexpensive, reliable, and dependable desalination method that can compete with the main conventional technologies. For example, the utilization of MD technologies in the purification of brackish and seawater has been extensively studied, experimentally, and theoretically [3,4,10,11,14,15]. Different approaches, such as integrating the MD modules with heat recovery devices [9,16,17], recirculating brine to magnify R_c [18,19], and adopting the multistage concept [16,20] were proposed and assessed to enhance the MD performance. Many researchers have considered the hybridization of MD with low-grade energy resources [21–23]. Recently, researchers began to address the dynamic modeling and transient analysis of its process [24–27]. These studies can be considered among the pioneers in the development of fundamental mathematical equations to describe the unsteady-state behaviors of standard MD processes. Ali et al. [28] and Ali et al. [29] compared different structures of the transient models. Nevertheless, most of the reported works in this regard were focused on developing, validating, and testing the transient models. It is valuable to further study the dynamic behavior of the MD process that enhances its operation and performance. For example, one can design optimal feed trajectories, implement safe startup and shutdown procedures, optimally operate the unit, employ fluctuating and/or intermittent energy sources, and design and apply robust control systems to reject unforeseen disturbances. Conversely, operating a pressure-driven membrane process, such as RO, employing a cyclic regime, results in enhanced mass flux [30]. This can be ascribed to the fact that a fluctuating flow rate or pressure promotes turbulence and contributes to the decrease of the concentration polarization and fouling [31–33]. Gustafson et al. [34] studied the effect of an intermittent energy source on MD performance. However, their study focused on the process structure and employed a steady-state model. In MD processes, both the concentration and temperature polarizations degrade their performance. However, according to Diez and Gonzalez [35], the temperature polarization exerts a significant influence on the mass transfer while the concentration polarization exerts a negligible impact. Inspired by the success of cycling the flow rate for RO performance, it was fitting to apply the same strategy to suppress the effect of temperature polarization (TPC) on the MD mass flux. Equally interesting to investigate whether the forced input changes affect the concentration polarization (CP) as in the RO process.

Most studies focus on the steady state behavior ignoring the dynamic variation of the performance due to the inherent internal transient lag of the process. The internal dynamic lag stems from the length of the module and interrelated mass and heat transfer phenomena. The dynamic lag may propagate when adding the external lag induced by piping and instrumentation hence degrading the performance during the transient. Ignoring the effect of dynamics may lead to the erroneous design of the power system which is characterized by transient behavior such the solar and wind energies. Therefore, the scope of this work is to study the effect of unsteady alternating inputs on the MD process to assess its dynamic behavior and performance which help identify the best operational practice and highlight the operating conditions that may degrade its performance. Moreover, this work aims at improving the temporal process performance utilizing periodic input functions. The input fluctuation may act as a turbulence promotor and mitigate the impact of poor mixing and temperature polarization similar to the concept of adding baffle and/or spacer [36,37].

2. Dynamic model of the MD process

The detailed formulation of an unsteady-state model of the DCMD unit was developed and validated in previous works [28,29,38]. Hence, only a summary of this model will be presented here. Basically, the dynamic model was developed by considering the unsteady-state heat balance around a hypothetical cell (Fig. 1a). Therefore, considering that the MD module (Fig. 1b) consists of n homogeneous, equally sized cells, the following mathematical expression could be written for the entire cells [28,29,38]:

$$\left(\frac{v}{n}\right)\rho C_p \frac{dT_{h_i}}{dt} = m_i C_p \left(T_{h_{i-1}} - T_{h_i}\right) - \left(j_{w_i} h_{v_i} + h_{m_i}\left(T_{h_{m,i}} - T_{c_{m,i}}\right)\right)\Delta x l \tag{1}$$

$$\left(\frac{v}{n}\right)\rho C_p \frac{dT_{c_i}}{dt} = m_i C_p \left(T_{c_{i+1}} - T_{c_i}\right) + \left(j_{w_i} h_{v_i} + h_{m_i}\left(T_{h_{m,i}} - T_{c_{m,i}}\right)\right)\Delta x l \tag{2}$$

Assuming a pseudo-steady state (PSS), the water and salt balance could be written as follows:

$$m_{h_i} = m_{h_{i-1}} - m_{w_i} \tag{3}$$

$$m_{c_{i+1}} = m_{c_i} + m_{w_i} \tag{4}$$

$$C_{s_i} = \frac{C_{s_{i-1}} m_{h_{i-1}}}{m_{h_i}} \tag{5}$$

$$\left(i = 1, \cdots, n\right) \quad \text{for} \quad i = n \rightarrow T_{h_i} \equiv T_{h_{\text{out}}}; \quad T_{c_{i+1}} \equiv T_{c_{\text{in}}}$$

$$\text{for } i = 1 \rightarrow T_{h_{i-1}} \equiv T_{h_{\text{in}}}; T_{c_i} \equiv T_{c_{\text{out}}}; m_{h_{i-1}} = m_{h_{\text{in}}}; m_{c_i} = m_{c_{\text{in}}}; C_{s_{i-1}} = C_{s_f}$$

Note that $m_{h_{\text{in}}}$, $m_{c_{\text{in}}}$, $T_{h_{\text{in}}}$, $T_{c_{\text{in}}}$, and $C_{s_{\text{in}}}$ are the process inputs while $T_{h_{\text{out}}}$, $T_{c_{\text{out}}}$, and m_w are the process outputs.

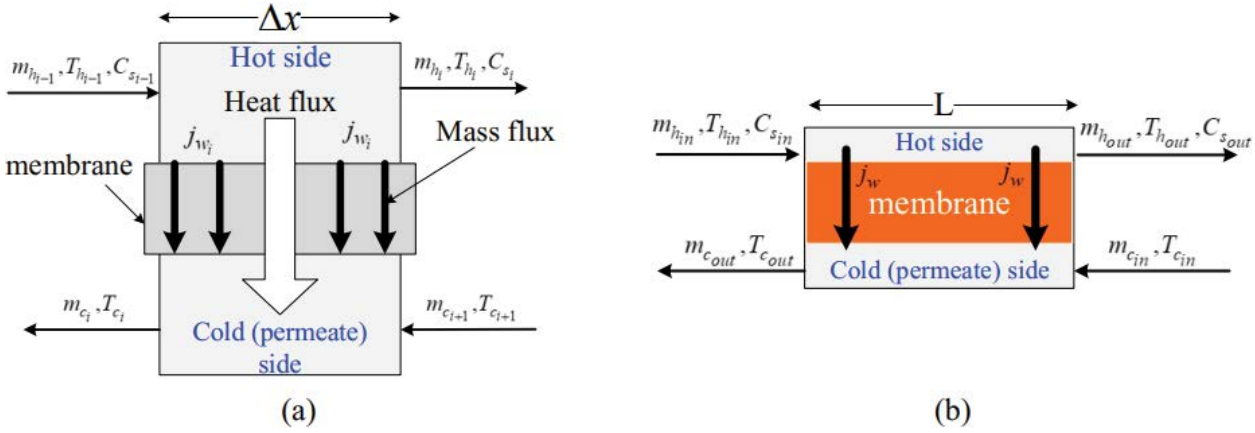

Fig. 1. Schematic of the MD process: (a) control volume and (b) whole module.

The feed salinity ($C_{s_{in}}$) was fixed, at 3 × 10^4 ppm and the cold feed temperature ($T_{c_{in}}$) was fixed at 20°C. Thus, the process featured three independent forcing inputs, namely $m_{h_{in}}$, $m_{c_{in}}$, and $T_{h_{in}}$, that control the process behavior and performance. The above dynamic model was solved numerically by the Euler method, employing the MATLAB software with the number of cells, n, is set to 10 in this study. The integration step size is set to 10 s, which was enough to afford a stable numerical solution. The experimental data of the previous work was employed to validate the model. In fact, the outlet temperatures were validated by Ali et al. [29,38] while the mass production was verified by Ali et al. [28]. The scope of this study was to utilize the validated models in the exploration of the transient behavior of the process. Notably, the numerical solution of the dynamic model requires an understanding of the intermediate variables, j_w, h_v, h_m, T_{h_w}, and T_{c_w} at each step size. These variables were determined by iteratively solving the combined mass and heat-transfer equations, as described in Appendix-A (in supplementary) and in [28,29,39]. After solving the MD model, the process performance was measured by the following key performance indicators: GOR, R_c, and TPC [3]:

$$\text{GOR} = \frac{m_w h_v}{m_{h_{in}} C_p \left(T_{h_{in}} - T_{\text{ref}}\right)} \tag{6}$$

$$R_c = \frac{m_w}{m_{h_{in}}} \tag{7}$$

$$\text{TPC} = \frac{T_{\text{hm}} - T_{\text{cm}}}{T_h - T_c} \tag{8}$$

where m_w and $m_{h_{in}}$ are the produced distillate and the feedwater flow rate, respectively, while h_v is the latent heat of vaporization.

The equations for the dynamic model [Eqs. (1)–(5)] do not explicitly rely on membrane characteristics. The underlying mass and heat-transfer equations, presented in Appendix-A (in supplementary), depend implicitly on the membrane sheet properties. The membrane properties employed here are as follows. The effective area is 10 m^2, the thickness is 230 mm, the channel length is 14 m, the channel height is 0.7 m, the pore diameter is 0.2 mm, and the porosity of 0.8.

The above model estimates the water production, based on the salt concentration of the bulk stream. This means that the vapor pressure of the hot channel, which was employed to compute the mass flux in Eq. (A9), was corrected by the bulk salinity [Eq. (A2)], implying that the concentration polarization was ignored. Actually, the solute that was transmitted with the water was blocked at the surface of the membrane surface (no permeation). The accumulated salt ions increased the salt concentration at the interface, compared to that at the bulk. Hence, the salt concentration at the membrane surface is given, as follows [35]:

$$C_w = C_s e^{\frac{J_w}{K\rho}} \tag{9}$$

where K is the mass-transfer coefficient of the solute. The latter was computed from the following correlation [35]:

$$\text{Sh} = 1.86\left(\text{ReSc}\frac{d_h}{L}\right)^{0.33} \tag{10}$$

where d_h is the hydraulic diameter, L is the channel length, and Re is the Reynold number. Further, the Schmidt and Sherwood numbers were defined as follows [35]:

$$\text{Sc} = \frac{\mu}{D\rho}; \quad \text{Sh} = \frac{Kd_h}{D} \tag{11}$$

where D is the diffusivity coefficient and μ the viscosity coefficient. Accordingly, the water vapor pressure [Eq. (A2)] that accounted for the concentration polarization can be modified as follows:

$$P_{1v} = \exp\left(23.238 - \frac{3{,}841}{T_{\text{hm}} - 45}\right)\left(1 - C_w\right)\left(1 - 0.5C_w - 10C_w^2\right) \tag{12}$$

and the corresponding mass flux Eq. (A9) is rewritten as follows:

$$m_v = j_v A = C_m \left(P_{1v} - P_2\right) A \tag{13}$$

Hence, to assess the effect of concentration polarization on the MD performance, m_v (mass flux influenced by concentration polarization is computed and compared to the nominal flux (m_w). We follow this approach here instead of computing CP itself. The numerical solution of the MD dynamic model can be explained by the algorithm shown in Fig. 2.

3. Forcing input scenarios

The separation mechanism in MD depends mainly on the internal heat transfer from the hot side to the cold side. This heat transport is complicated and considerably affected by the circulation rate and the temperature of the fluids. Circulation rate has a profound and dual impact on heat transfer. A high flow rate improves the heat transfer coefficient and simultaneously reduces the residence time. Similarly, high fluid temperature increases the driving force for heat transfer and vice versa. On top of that, the membrane sheet is lengthy and spiral such that during sudden changes in the feed temperature and/or flow rate, a non-homogeneous temperature profile may exist along the membrane module. The combination of these phenomena influences the transient heat transfer and consequently the process performance. Considering the external heat transfer of the powering system and/or heat recovery system, the situation becomes even more complicated. However, the external heat transfer is not considered here. Nevertheless, to evaluate the transient internal heat transfer on the MD performance, the following forcing inputs are designed and implemented.

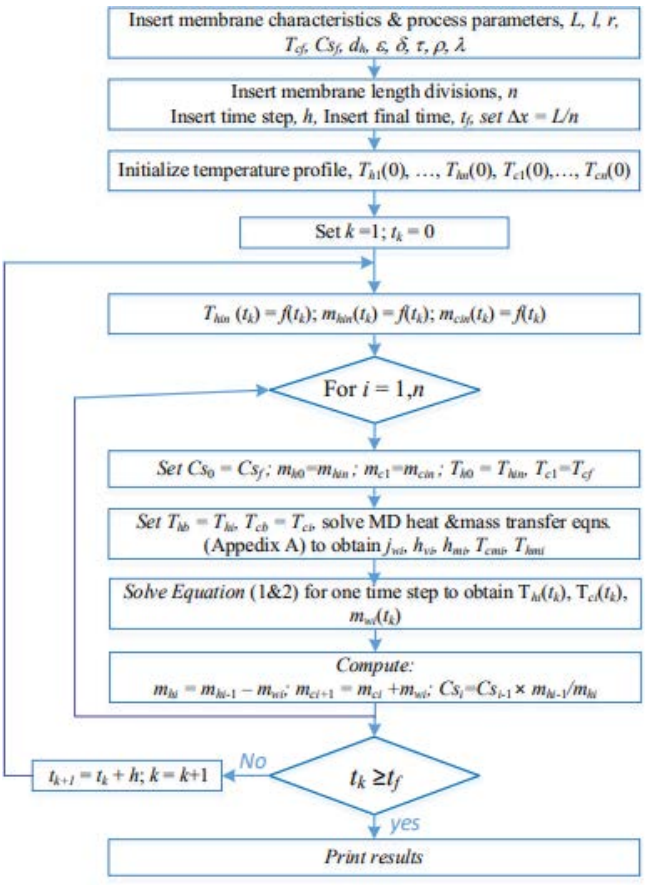

Fig. 2. Organigram for the MD dynamic model solution.

The focal analysis in this study relied on the dynamic response of the process with various forced input functions. To elucidate the discussion in the following sections, the various schemes of the forced input functions were described and presented in Table 1. All these input variations were tested, as would be discussed in the following subsections. Table 1 includes forcing inputs for the feed flow rate at constant feed temperature which are tagged by the letter "F" and forcing inputs for the feed temperature at constant feed flow rate tagged by the letter "T". For flow rate, the second and third letters of the tag name describe the status of the hot and cold streams, respectively as Constant, Ascending, Descending, Periodic, or Reverse Periodic. Reverse periodic means that the hot and cold streams are alternating in the opposite direction, that is, when the hot stream becomes at a high flow rate, the cold stream will be at the lowest flow rate and vice versa. For feed temperature, the second letter designates the status of the temperature as Ascending or Descending. The letter "L" appears at the end of any function tag indicates that the flow rate of the cold stream is at its lowest value of 100 L/h. The forcing input functions can be either a series of step changes or square waves. The train of steps is used to investigate the underlying dynamic characteristics of the process while the periodic functions are used to explore the process performance during such fluctuation.

4. Results and discussion

4.1. Effect of the feed flow rate

In this section, we analyzed the dynamic behavior of the MD module. Usually, the dynamic response is characterized by the fundamental time constant which measures the response speed. The time constant is determined by step-testing the major process inputs, namely the feed flow rates and the hot inlet feed temperature. First, we focused on the effect of varying the feed flow rates for both channels, at a fixed inlet feed temperature. Particularly, scenarios FDC, FDD, FAC, and FAA are tested. The illustration of the forced input profiles is shown in Fig. S1 (supplementary material). For all the scenarios, the hot inlet temperature was fixed at 80°C, and the inlet cold temperature at 20°C. FD's scenarios illustrate the start-up of the hot inlet feed flow, from zero to the highest flow rate (500 kg/h), followed by a stepwise reduction, at a constant step change (100 kg/h) and a fixed period (50 min). The cold inlet flow rate was either kept constant at 500 kg/h (FDC) or subjected to exactly the same periodic trend of $m_{h_{in}}$ (FDD). FA's scenarios depict the opposite input profiles, that is, the feed flow rate was increased by a step change of 100 kg/h for each 50 min. Similarly, the cold inlet flow rate could be either constant (FAC) or chronologically varied with the hot feed flow rate (FAA). It is common to maintain equal flow rates in both channels, although it is expected that

Table 1
Description of the different forced input functions

Case	$T_{h_{in}}$ (°C)	$m_{h_{in}}$ (kg/h)	$m_{c_{in}}$ (kg/h)
FCC	80	500	500
FAC	80	Ascending steps of 100 kg/h	500
FACL	80	Ascending steps of 100 kg/h	100
FAA	80	Ascending steps of 100 kg/h	Ascending steps of 100 kg/h
FPC	80	Periodic between 500 and 100, with p_r = 10 min	500
FPP	80	Periodic between 500 and 100 with p_r = 10 min	Period between 500 and 100 with p_r = 10 min
FPR	80	Periodic between 500 and 100 with p_r = 10 min	Period between 100 and 500 with p_r = 10 min
FDC	80	Descending steps of 100 kg/h	500
FDD	80	Descending steps of 100 kg/h	Descending steps of 100 kg/h
TD/TDL	Descending steps, at 10°C	500/100	500/100
TA/TAL	Ascending steps, at 10°C	500/100	500/100

an unbalanced flow rate may improve the performance. For example, Naidu et al. [40] reported a 30% enhancement of R_c when a cold to hot flow ratio of 1.375 was utilized. The response of the average bulk temperature for both membrane channels to these input scenarios is shown in Fig. 3. Notably, the bulk temperature (Fig. 3) is the average value of the bulk temperatures along the membrane length. When both feed flow rates varied chronologically, the temperature response became symmetric. The estimated time constants for the ascending or descending step changes are constant, ~3 min, as listed in Table 2 for fixed $m_{c_{in}}$. The time constant was estimated from the time responses, employing the reaction curve method [41]. Clearly, a minor variation in the estimated time constant was related to the accuracy of the calculation procedure. This calculation was affected by the integration step size, 10 s, in this study. The resemblance of the computed time constant indicated that the response speed was unaffected by the operating condition, namely the same step-change size. Moreover, the dynamic behavior was linear as the time constant remained almost constant regardless of the input trajectory, that is, ascending or descending. However, when both feed flow rates varied sequentially, the time constant changed with the operating conditions, as listed in Table 2. In that case, the process dynamic became as slow as 8 min, at a lower flow rate. When $m_{c_{in}}$ was constant, the process dynamic depended only on the variation of the hot feed flow rate. Conversely, when both feed flow rates were alternated, the heat-transfer mechanism changed accordingly, resulting in variable dynamic behaviors. The effect of the low feed flow rate on the dynamics was evident, as shown in Fig. 2c and d, during startup operation. In Fig. 3c, the inlet flow rate of the cold side was very high during the startup, compared to the hot inlet flow rate, thereby causing rapid heat transfer, and thus a rapid evolution of the bulk temperatures. However, as shown in Fig. 3d, both inlet flow rates were very low (100 kg/h) at the startup interval, thereby decelerating the response time significantly. The input profile (Table 1) was also applied to the MD process but at a fixed hot inlet temperature of 50°C. The graphical results are not displayed to limit the number of figures. The obtained time constants of the descending step changes are listed in Table 2. At a high fixed value of $m_{c_{in}}$, the response speed was similar to that at a fixed hot inlet temperature of 80°C. This indicated that a high inlet flow rate for the cold stream controls the dynamics of the process. However, when tandem feed flow rates were applied, the dynamic response became faster manifested by a time constant of 20 s. Actually, the response became faster than when the same feed strategy was employed, although at a high hot inlet temperature (80°C). Moreover, the time constant became independent of the operating condition of the flow rate. At very low operating temperatures, such as at 50°C, the driving force (temperature difference) became smaller, hence the fluid circulation became less effective. This phenomenon was discussed in earlier works [29,38].

Further, we studied the physical behavior of the MD process, as illustrated in Fig. 4. The insight performance of the response, shown in Fig. 3b (synchronized feed flow rates), is depicted in Fig. 4. Fig. 4a shows the time evolutions of TPC, at selected locations along the membrane length, that is, 10%, 30%, etc. Moreover, Fig. 4b–e illustrate the axial trend of the bulk temperature and mass flux, at the two steady-state points; the highest and lowest flow rates, 500 and 100 kg/h, respectively. As shown in Fig. 4b, the difference of the bulk temperatures, as well as that at the interface temperatures between the hot and cold channels is wider at 500 kg/h than that at a lower one (100 kg/h). The wider temperature difference caused a larger mass flux, as shown in Fig. 4d because the mass flux was proportional to the temperature difference. Conversely, the temperature difference, at a lower operating temperature was narrower, resulting in a smaller mass flux, as illustrated in Fig. 3c and e. Evidently, the temperature difference diminished as the flow rate decreased. This phenomenon can be explained as follows: as the fluid circulation reduces, the heat losses to the surrounding emerges in the hot channel [40,41]. Furthermore, the heat losses due to conduction resistance dominated the heat-transfer mechanism. Consequently, the bulk temperature of the hot stream shifted to a smaller value, at the exit point. Contrarily, the reduced flow rate increased the residence time, allowing the cold stream to absorb more heat. The combination of these effects resulted in a narrowed temperature difference,

as depicted in Fig. 4c. The low exit temperature of the hot stream, at a low flow rate, reduced the average value of the hot stream, compared to that, at a high flow rate. Similarly, the higher exit temperature for the cold stream, at a low flow rate, increased the average value of the cold stream, compared to that, at a high flow rate. This behavior explains the narrowing and symmetric temperature trends shown in Fig. 3b. Fig. 4a demonstrates a relatively large value for TPC (>0.6) along the MD module, indicating the negligible effect of the temperature polarization due to enhanced heat transfer in both channels. However, TPC became slightly lower and exhibited a broader distribution at the lowest feed flow rate. As mentioned earlier, at the lowest flow rate, the conduction resistance began to prevail, causing a slight degradation of the heat-transfer mechanism, at the membrane interface. Considering the average value of TPC along the membrane length, a 3% change in TPC, between $m_{h_{in}} = 500 \frac{kg}{h}$ and $m_{h_{in}} = 100$ kg/h, exerted a tremendous impact on the mass flux, as depicted in Fig. 3d and e.

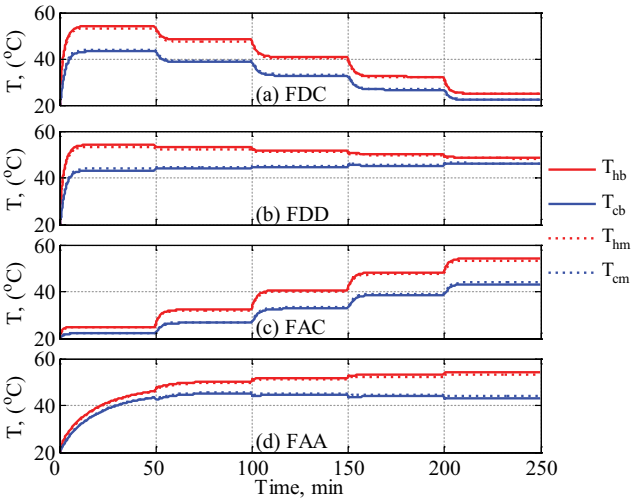

Fig. 3. The time response of the average bulk temperature to different input scenarios.

Fig. 5 displays the physical insight of the process response shown in Fig. 3a. This illustration corresponds to the input strategy involving periodically descending $m_{h_{in}}$ while $m_{c_{in}}$ was kept constant at a high value of 500 kg/h. The bulk temperature and mass flux profile, at the highest flow rate (Fig. 4b and d), resembled those shown in Fig. 3b and d because $m_{c_{in}}$ coincided with $m_{h_{in}}$ in both cases. When the hot inlet flow rate approached the minimum, an exotic profile of the bulk temperature along the membrane length was observed, as shown in Fig. 5c. Because the flow rate of the cold stream was very high, compared to that of the hot stream, the MD module functioned as a heat exchanger. Moreover, the cold stream rapidly quenched the hot fluid and eliminated the heat-transfer process and evaporation. Subsequently, the mass flux became zero for $x/L > 0.5$, as shown in Fig. 5e. The trend of the bulk temperatures along the membrane length (Fig. 5c) reduced their corresponding average value as the feed flow rate decreased. This explains the simultaneous reductions in both bulk temperatures when the flow rate was decreased, as shown in Fig. 3a. Fig. 5a shows that TPC remains high, at all the flow rates, thus indicating that a well-designed module had been developed. As the flow rate decreased, TPC became slightly higher and narrower, thereby rendering the mass-transfer process more limited. The narrow and saturated TPC, at lower flow rates, reflected the temperature profile shown in Fig. 5c. Furthermore, the TPC response in

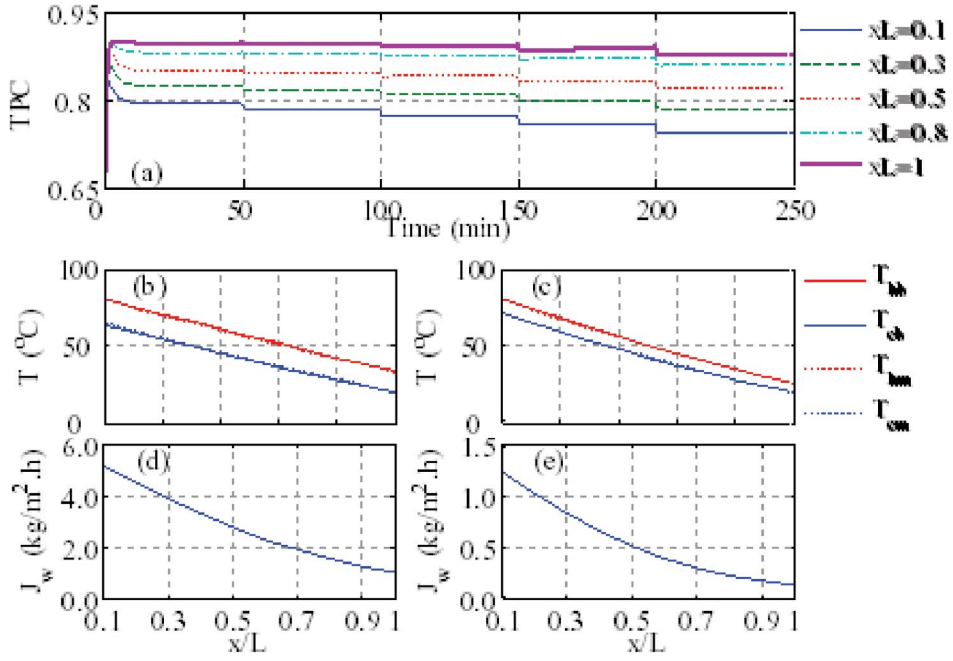

Fig. 4. Process behavior of the synchronized descendings of both feed flow rates (FDD): (a) dynamic TPC, (b and d) steady-state temperature and flux profile, at $m_{h_{in}} = m_{c_{in}} = 500$ kg/h, (c and e) steady-state temperature and flux profile, at $m_{h_{in}} = m_{c_{in}} = 100$ kg/h.

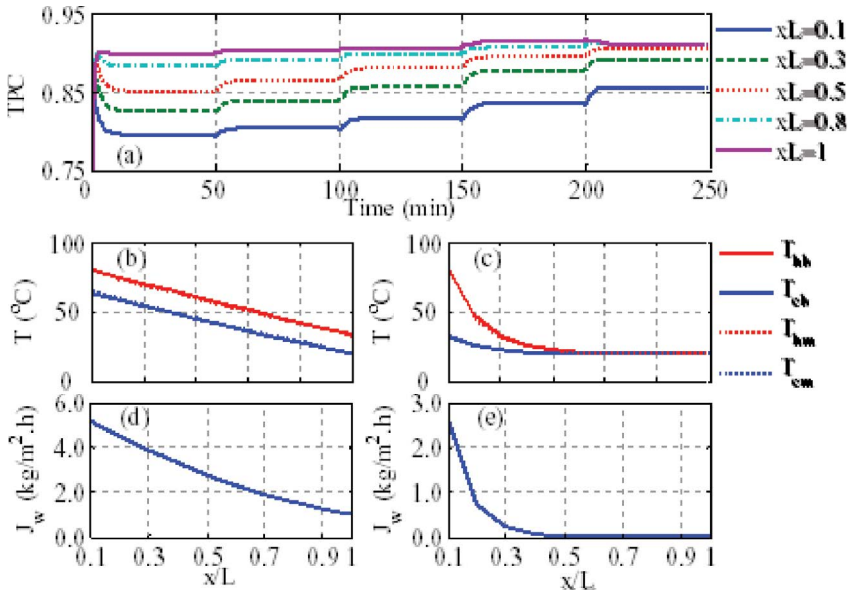

Fig. 5. Process behavior for the descending $m_{h_{in}}$ and fixed $m_{c_{in}}$ (FDC): (a) dynamic TPC, (b and d) steady-state temperature and flux, at $m_{h_{in}} = m_{c_{in}} = 500$ kg/h, (c and e) steady-state temperature and flux, at $m_{h_{in}} = 100$ kg/h, $m_{c_{in}} = 500$ kg/h.

this case (FDC) exhibited a transient behavior, compared to that in (FDD), which coincided with the temperature response, as shown in Fig. 3. As aforementioned, the reason for the apparent dynamic is the unbalanced feed flow rates. According to the above findings, increasing the cold flow rate to many folds of the hot stream was not recommended, especially for long modules. Consequently, an excess of the cold stream, relative to the hot stream, should be avoided in long membranes because it could result in a negative mass flux. Ali et al. [13] reported that a positive driving force could not be attained over the module length or a conceptually large number of sequential MD stages.

4.2. Effect of the inlet feed temperature

Next, the effect of the hot inlet temperature on the process dynamics was examined for the scenarios listed in Table 2. The illustration is shown in the supplementary material as Fig. S2. For the high flow rate, the reported value of the time constant listed in Table 2, indicated that the process dynamic was unaffected by the operating temperature or the step-change mode, that is, ascending or descending. Conversely, at a low flow rate of 100 kg/h, the response of the process became very sluggish, as indicated by large time constants listed in Table 2. This result illustrates that frequent alteration of the feed flow rate has more effect on the process dynamics and performance than feed temperature. This is because the fluid velocity influences the fluid hydrodynamics and heat-transfer mechanisms.

4.3. Effect of concentration polarization

As mentioned earlier, the concentration polarization exerted a negligible effect on MD performance. Nevertheless, the fluid turbulence generated by the fluctuation of the flow could disturb the polarization layer. Hence improvement in the mass flux was expected. To assess this proposition, the system performance in the rectangular wave of the feed flow (FPP) was tested. Fluctuation in the flow of the hot channel is enforced because it carries the salt ions. Symmetrical flow alteration in the cold channel was implemented to afford consistent process performance, as discussed in the previous tests. The outcome of the test is depicted in Fig. 6. The transient behavior of the average salt concentration of the bulk and membrane walls is demonstrated in Fig. 6a. The feed flow exerted a minor impact on the bulk salt concentration. Although the variation in C_s with flow exits was negligible, it was obscured by the large scale of the plot. Actually, the salt concentration of the bulk was mainly influenced by the water recovery. Since the latter was low for single-pass operation, an increase in C_s remained negligible. Despite the apparent changes in the mass flux (m_w) with the flow, as shown in Fig. 6b, its effect on the bulk salt concentration remained trivial. Conversely, the salt concentration, at the membrane surface (C_w) was higher in magnitude, as expected, and it varied evidently with the flow rate. The dependence of C_w on the flow was intuitive because the flow circulation enhanced the fluid hydrodynamics, and hence the mass transfer of the solute from the bulk to the membrane walls. This was more evident as C_w grew, at higher flow rates. Nevertheless, the impact of the concentration polarization on the mass flux (m_v), which was computed, employing the salt concentration at the membrane wall, was minor, as shown in Fig. 6b. Therefore, we concluded, as also noted by Diez and Gonzales [35], that the concentration polarization exerted a minor impact on the performance of MD.

4.4. Periodic operation of the process

As already discussed, the flow rate was effective in the process dynamics, as well as on TPC, and hence on the

Table 2
Time constant of the temperature response for different flow/temperature scenarios

Case	T = 80°C $m_{c_{in}}$ = 500 kg/h		T = 80°C $m_{c_{in}} = m_{h_{in}}$		T = 50°C $m_{c_{in}}$ = 500 kg/h	T = 50°C $m_{c_{in}} = m_{h_{in}}$
$m_{h_{in}}$ (kg/h)	FDC	FAC	FDD	FAA	FDC	FDD
0–500	2.17 min	1.33 min	2.2 min	14.5 min	2.17 min	2.17 min
500–400	2.83 min	2.83 min	1.0 min	0.8 min	2.83 min	0.33 min
400–300	3.17 min	3.00 min	2.3 min	1.5 min	3.17 min	0.33 min
300–200	3.00 min	2.50 min	4.8 min	3.0 min	3.17 min	0.33 min
200–100	2.33 min	2.50 min	7.7 min	8.0 min	2.50 min	0.33 min
Case	$m_{h_{in}} = m_{c_{in}}$ = 100 kg/h			$m_{h_{in}} = m_{c_{in}}$ = 500 kg/h		
$T_{h_{in}}$ (°C)	TDL			TD		TA
20–80	17.17 min			2.17 min		2.17 min
80–70	17.33 min			2.33 min		2.33 min
70–60	18.67 min			2.33 min		2.33 min
60–50	18.83 min			2.33 min		2.33 min
50–40	18.33 min			2.33 min		2.17 min

overall performance. Additionally, it is believed that the periodic forcing of the pressure and/or flow rate could positively affect the membrane performance in RO processes. It was reported that the frequent alteration of the flow rate affected the concentration polarization of the membrane boundary layer and improved the mass transfer. In the MD process, the concentration polarization exerted less effect than the temperature polarization. Indeed, the fluctuation of the fluid circulation exerted some effects on TPC, as discussed above. Thus, by analogy, the periodic forcing of the feed flow rate was expected to influence TPC and the overall performance of the MD process. Therefore, this section is focused on studying the impact of a periodic feed flow rate scenario, mainly in the form of square waves, on the performance of MD. Nevertheless, the hot inlet temperature was fixed at 80°C. The result is shown in Fig. 6.

In these figures, the MD process was simulated, utilizing different flow rate scenarios. Case (FCC) referred to fixed hot and cold flow rates, at 500 kg/h, case (FPC) referred to fixed cold flow rates, at 500 kg/h while the hot stream oscillated between 100 and 500 kg/h, at a fixed period of 10 min, case (FPP) referred to both cold and hot streams that oscillated simultaneously at the same amplitude and period as the case (FPC). In case (FPR), the hot stream fluctuated in the same fashion, as in case (FPC), while the cold stream fluctuated at the same amplitude and period as in case (FPC) but in the opposite direction. Case (FCC) will be selected as the nominal situation to compare the other feed

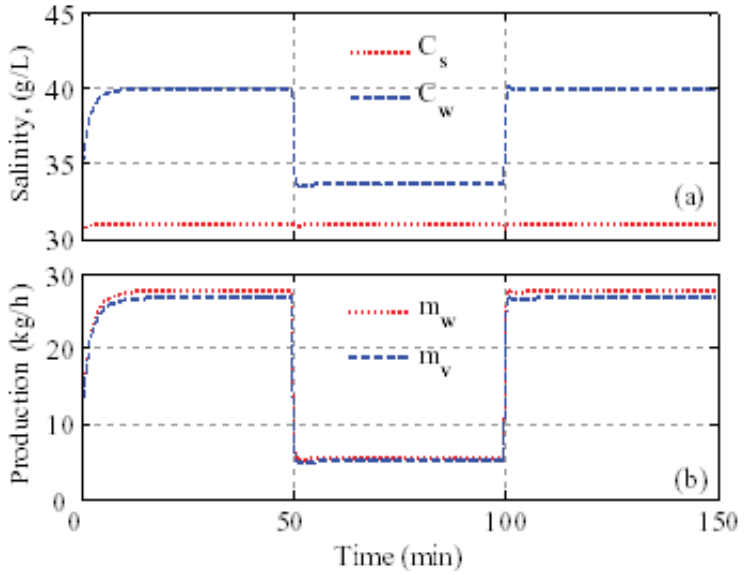

Fig. 6. Effect of the forced input (FPP) on salinity and water production.

strategies. This is to assess whether another feed scenario could improve the performance beyond the nominal case. Fig. 7a–c depict the raw instantaneous response of the production rate, GOR, and R_c. The instantaneous behavior of these key variables displayed overlapping trends. Hence, for better visualization and fair comparison, these variables were presented in terms of accumulative modes, as shown in Fig. 7e–g. Intuitively, the production rate in the nominal case outperformed the other strategies. However, considering GOR and R_c, the outcome was reversed because the average value of the hot feed flow rate was less than that for the nominal case. Notably, by definition, GOR and R_c are inversely proportional to the hot feed flow rate [Eqs. (6) and (7)]. Undoubtedly, when a counter cyclic operation was enforced, the best performance in terms of high GOR and R_c was observed, as shown in Fig. 6f and g. Thus, by cyclic operation, we could achieve high production and consume less energy per feed resource. Noteworthily, the superiority of the case (FPR) over the case (FPP) was not due to the low average value of the flow rate of the hot stream because that was common in both cases. The enhancement was ascribed to the dynamic behavior of the process during the periodic operation with opposite directions (i.e., case FPR), which affected the mass and heat transfer of the membrane, and resulted in different mass flux profiles, as shown in Fig. 7a. To further explain this, we compared the performance of cases (FPP) and (FPR) as illustrated in Fig. 8.

The bulk-temperature response to the harmonious cyclic wave in the feed flow rates is shown in Fig. 8a. The variation in the hot and cold bulk temperatures with a fluctuating flow rate was discussed earlier. The bulk-temperature response to the opposite cyclic waves in the feed flow rates is depicted in Fig. 8b. It was clear that an alteration of the flow rate of the cold stream dramatically influenced the dynamic behavior of the bulk temperature. Within a short period (10 min), the bulk temperature could not attain a steady state because of the large difference between the flow rates of the two streams. This ramp response generated the saw-like temporal trend of the bulk temperature, as shown in Fig. 8b. Moreover, when $m_{h_{in}}$ was high and $m_{c_{in}}$ low, the latter was rapidly heated, and when $m_{h_{in}}$ was low and $m_{c_{in}}$ high, the former was rapidly cooled. This is because their corresponding heat-transfer coefficients exhibited large deviance. Thus, the cold bulk temperature fluctuated between two large extreme values, compared to that of the hot stream (Fig. 8a). This interesting trend of the bulk temperatures incurred a disturbance at the membrane boundary layer, generating a wide distribution of TPC along the membrane length, as exhibited in Fig. 8d. Thus, the scrambled TPC resulted in the distinguished time evolution of the mass flux, as manifested in Fig. 8e. Notably, the mass flux of the synchronized flow rates (case (FPP)) flipped sharply between two extreme values within each wave period. Conversely, the mass flux for the non-harmonized flow rates exhibited a wider range of values within each period. Despite its smaller value, compared to that of the case (FPP), the higher mass flux resulted in higher GOR and R_c values, as shown in Fig. 6b and c, and consequently resulted in larger accumulated values, as shown in Fig. 6f and g. The process behavior in Figs. 7 and 8 display the role of the transient behavior on the performance. The transient behavior is governed by the time constant, that is, speed of response. For example, GOR and R_c in Fig. 7b and c exhibit spikes for periodic flow rate although the mass production is low. This is because, at the moment when the flow rate is stepped down, the average membrane temperature is temporarily still high because the temperature changes gradually along the membrane length. This high average value for temperature creates a relatively large mass flux. Hence, R_c and GOR which are proportional to the mass flux and inverse proportional to the feed flow rate become high at that instant. However, these peaks deplete rapidly for the FPP case because its dynamic is fast causing the average temperature to change quickly with changing flow rate as shown in Fig. 8a. However, for FPC and FPR cases where the cold stream flow rate is different than that of the hot stream,

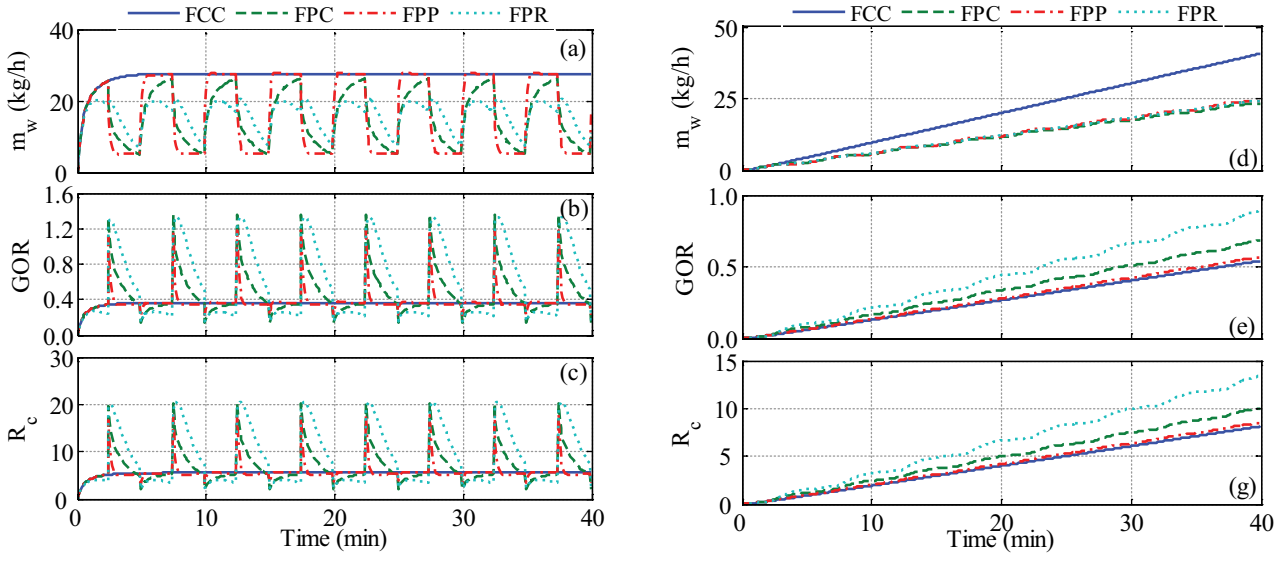

Fig. 7. Dynamic response of KPI to various forced periodic inputs.

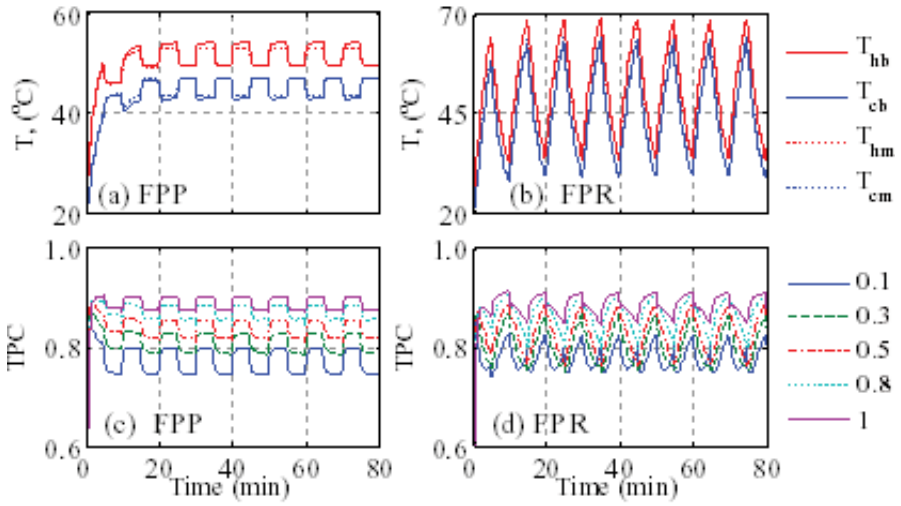

Fig. 8. Comparison of cases (FPP) and (FPR).

the situation is different. In these cases, the different flow rates cause slower dynamics for the heat transfer as well as the average membrane temperature as shown in Fig. 8b. The gradually changing temperature leads to slowly changing mass flux as shown in Fig. 8e. As a result, the ratios, GOR and R_c depleted slowly as shown in Fig. 7b and c.

We further highlighted the effect of the period of oscillation on the feed flow rates (Fig. 9). The figure displayed the variation in the key parameters of the process, that is, the accumulated GOR and R_c with the period of oscillation of the cold stream flow (f_c), at selected values for a period of oscillation of the hot stream (f_h). Specifically, the maximum value of the key parameters was plotted. Since the scope here is the accumulated values, the maximum value corresponded to the value at the end of the simulation time, as indicated by Fig. 6e–g. Generally, the process performance, in terms of GOR and R_c, decreased as f_h increased. Similarly, the performance degraded as f_c increased. Interestingly, the maximum performance was observed where f_c coincided with f_h, which was clear, for $f_h = f_c$ = 1,5,10. When f_h increased, the span of half of the period became long enough for the temperature response to approach a steady state. This reduced the intensity of the disturbance that was induced by the frequent fluctuations on the boundary layer of the membrane sheet, thereby degrading the performance. When f_c departed from f_h, the forced input function became similar to that of (FPC), that is, a periodic $m_{h_{in}}$ and an almost constant $m_{c_{in}}$. Here, $m_{c_{in}}$ remained either low or high for an extended duration, hence causing the degradation of the mass flux. For f_c shorter than f_h, the fluctuation in $m_{c_{in}}$ became aggressive, causing the resulting disturbance on the membrane interface to be short-lived. Subsequently, the performance enhancement did not increase as intended. The figure also shows the comparison of the resulted performances to that of the baseline, that is, when $m_{h_{in}} = m_{c_{in}} = 500$ kg/h. Clearly, the GOR performance was inferior to the baseline as f_h and f_c escalated. Contrarily, the performance of R_c was more reasonable over the f_c range. However, the extent to which GOR deteriorated varied with f_h. For example, as f_h increased, the successful

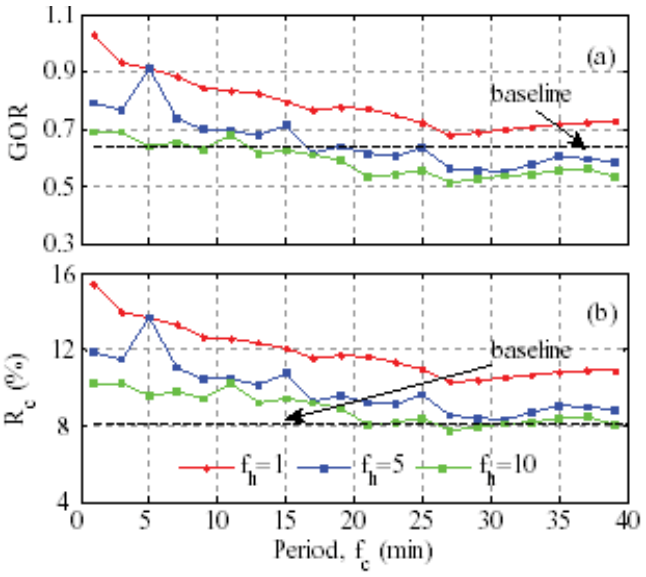

Fig. 9. Effect of cycle period on the process performance.

range of f_c decreased. For f_h = 1 min, GOR was almost above the baseline while R_c was above the baseline for the whole range of f_c. Further, for f_h = 5 min, the positive GOR was up to f_c = 15 min while R_c remained almost acceptable over the whole span. For f_h = 10 min, GOR could be effective, only at very low f_c, for up to 3 min or at the maximum, that is, f_c = 10 min. Conversely, R_c remained effective for up to an oscillation period of 20 min, after which it fluctuated around the nominal value.

It should be noted that the improved performance due to input fluctuation is also achieved at lower energy consumption. The average feed flow rate of the parodic pulses is 300 L/h (maximum 500 and minimum 100 L/h) which is 60% of operating at a fixed feed flow rate of 500 L/h. Note that the pumping energy and heating energy (sensible heat of the feed) is proportional to the feed flow rate. Therefore, the ratio of the consumed energy when operating periodically

to that when operating at a fixed feed flow rate is also 60%. This means 40% saving in the consumed energy is achieved.

5. Conclusions

An experimentally validated dynamic model for DCMD was developed to study the process behavior and performance, under forced input changes. The forced inputs were the hot stream flow rate, the cold stream flow rate, and the inlet hot temperature. The primary outputs were the bulk temperature of the cold and hot streams. The simulation indicated the linearity of the transient response of the bulk temperatures to chronologically fixed-step changes in both feed flow rates. This is substantiated by the consistent speed of response, regardless of the operating conditions and direction of the step changes. However, the process dynamics became very slow, at very low feed flow rates (100 kg/h). This was attributed to the poor heat-transfer mechanism due to the domination of heat. It was confirmed that fixing or altering the cold stream in opposite directions to the hot stream exerted a profound effect on the process dynamics and performance. This is because the independent alteration exerted an acute influence on the heat-transfer mechanism. It was also observed that periodic operation of MD with a train of opposite pulses for the feed flow rates with similar amplitudes and periods of oscillation enhances the accumulated GOR and R_c by almost 100%. Further, decreasing the period of both the hot and cold stream cycles maximized the reported improvement. The performance enhancement by cycling operation can be attributed to the effect of the periodic circulation on temperature polarization. However, concentration polarization showed a minor effect on the MD performance.

Acknowledgment

This project is funded by the Researchers Supporting Project number (RSP2022R510), King Saud University, Riyadh, Saudi Arabia.

Symbols

A	—	Cross-sectional area, m^2
C_m	—	Permeability coefficient, kg/m^{2}s Pa
C_m^k	—	Knudsen mass flux coefficient, kg/m^{2}s Pa
C_m^d	—	Molecular diffusion mass flux coefficient, kg/m^{2}s Pa
C_m^c	—	Transition mass flux coefficient, kg/m^{2}s Pa
C_p	_	Heat capacity, J/kg K
C_s	—	Salt concentration, at the bulk, %
C_w	—	Salt concentration, at the membrane surface, %
d_e	—	Collision diameter of the water vapor and air, m^2
d_h	—	Hydraulic diameter, m
D	—	Diffusivity coefficient, m^2/s
f_h	—	Period of oscillation for the hot stream, min
f_c	—	Period of oscillation for the cold stream, min
GOR	—	Gain output ratio
h_v	—	Latent heat of vaporization, J/kg
h_f, h_p, h_m	—	Feed, permeate, and membrane heat-transfer coefficients, W/m^2 K
J_w	—	Mass flux, kg/m^{2}h
J_v	—	Mass flux based on the concentration polarization, kg/m^{2}h
k_B	—	Boltzmann's constant
k_m	—	Membrane conductivity, W/m K
k_s	—	Solid-phase thermal conductivity, W/m K
k_g	—	Gas-phase thermal conductivity, W/m K
k_n	—	Knudsen number
K	—	Mass-transfer coefficient for the solute, m/s
l	—	Channel height, m
L	—	Channel length, m
m	—	Mass flow rate, kg/h
m_w	—	distillate flow rate, kg/h
m_v	—	Distillate flow rate based on the concentration polarization, kg/h
M_w	—	Molecular weight
Nu	—	Nusselt Number
n	—	Number of membrane length divisions, that is, the control elements
P_1, P_2	—	Vapor pressure at the feed and permeate membrane surfaces, Pa
P_{1v}	—	Vapor pressure at the feed membrane surface, based on the concentration polarization, Pa
P	—	Average membrane interface pressure, Pa
P_a	—	Entrapped air pressure, Pa
PD	—	Membrane pressure multiplied by diffusivity, Pam^2/s
Pr	—	Prandtl number
p_r	—	Period of oscillation
r	—	Membrane pore size, m
R	—	Ideal gas constant
R_c	—	Recovery ratio
Re	—	Reynold Number
t	—	Time
T_h, T_c	—	Feed (hot) and permeate (cold) temperatures, K
T_{hb}, T_{cb}	—	Feed (hot) and permeate (cold) bulk temperatures, K
T_{hm}, T_{cm}	—	Feed and permeate membrane temperatures, K
$T_{h_{out}}$, $T_{h_{in}}$	—	Outlet and inlet hot feed temperatures, °C
$T_{c_{out}}$, $T_{c_{in}}$	—	Outlet and inlet cold stream temperatures, °C
T	—	Average temperature, at the membrane interface, K
U	—	Overall heat-transfer coefficient, W/m^{2}K
v	—	Channel volume, m^3

Greek

α	—	Tuning parameter
τ	—	Tortuosity
ρ	—	Water density, kg/m^3
δ	—	Membrane thickness
ε	—	Porosity
λ	—	Mean free path, m
μ	—	Viscosity coefficient, Pa/s
Δx	—	Control volume

Subscript

i	—	Control element, i
c	—	Cold stream
h	—	Hot stream

References

[1] M.W. Shahzad, M. Burhan, K.C. Ng, A standard primary energy approach for comparing desalination processes, npj Clean Water, 2 (2019) 1–7, doi: 10.1038/s41545-018-0028-4.

[2] N. Ghaffour, S. Soukane, J.-G. Lee, Y. Kim, A. Alpatova, Membrane distillation hybrids for water production and energy efficiency enhancement: a critical review, Appl. Energy, 254 (2019) 113698, doi: 10.1016/j.apenergy.2019.113698.

[3] D. González, J. Amigo, F. Suárez, Membrane distillation: perspectives for sustainable and improved desalination, Renewable Sustainable Energy Rev., 80 (2017) 238–259.

[4] M. Khayet, Desalination by Membrane Distillation, Encyclopedia of Life Support Science (EOLSS), Water and Wastewater Treatment Technologies, Encyclopedia of Life Support Systems (EOLSS), Paris, France, 2010.

[5] Y. Lu, J. Chen, Optimal design of multistage membrane distillation systems for water purification, Ind. Eng. Chem. Res., 50 (2011) 7345–7354.

[6] J. Minier-Matar, A. Hussain, A. Janson, F. Benyahia, S. Adham, Field evaluation of membrane distillation technologies for desalination of highly saline brines, Desalination, 351 (2014) 101–108.

[7] Q.L. Ve, K. Rahaoui, M. Bawahab, H. Faqeha, A. Date, A. Akbarzadeh, M.C. Do, Q.L. Nguyen, Experimental investigation of heat transfer correlation for direct contact membrane distillation, J. Heat Transfer, 142 (2020) 012001, doi: 10.1115/1.4044707.

[8] J. Phattaranawik, R. Jiraratananon, Direct contact membrane distillation: effect of mass transfer on heat transfer, J. Membr. Sci., 188 (2001) 137–143.

[9] E.K. Summers, H.A. Arafat, J.H. Lienhard V, Energy efficiency comparison of single-stage membrane distillation (MD) desalination cycles in different configurations, Desalination, 290 (2012) 54–66.

[10] D.U. Lawal, A.E. Khalifa, Flux prediction in direct contact membrane distillation, Int. J. Mater. Mech. Manuf., 2 (2014) 302–308.

[11] K. Nakoa, A. Date, A. Akbarzadeh, A research on water desalination using membrane distillation, Desal. Water Treat., 56 (2015) 2618–2630.

[12] L.M. Camacho, L. Dumée, J. Zhang, J.-d. Li, M. Duke, J. Gomez, S. Gray, Advances in membrane distillation for water desalination and purification applications, Water, 5 (2013) 94–196.

[13] A. Ali, J.-H. Tsai, K.-L. Tung, E. Drioli, F. Macedonio, Designing and optimization of continuous direct contact membrane distillation process, Desalination, 426 (2018) 97–107.

[14] Ó. Andrjesdóttir, C.L. Ong, M. Nabavi, S. Paredes, A.S.G. Khalil, B. Michel, D. Poulikakos, An experimentally optimized model for heat and mass transfer in direct contact membrane distillation, J. Heat Mass Transfer, 66 (2013) 855–867.

[15] D. Winter, J. Koschikowski, M. Wieghaus, Desalination using membrane distillation: experimental studies on full scale spiral wound modules, J. Membr. Sci., 375 (2011) 104–112.

[16] E. Drioli, A. Ali, F. Macedonio, Membrane distillation: recent developments and perspectives, Desalination, 356 (2015) 56–84.

[17] G. Guan, X. Yang, R. Wang, A.G. Fane, Evaluation of heat utilization in membrane distillation desalination system integrated with heat recovery, Desalination, 366 (2015) 80–93.

[18] H.C. Duong, P. Cooper, B. Nelemans, T.Y. Cath, L.D. Nghiem, Optimising thermal efficiency of direct contact membrane distillation by brine recycling for small-scale seawater desalination, Desalination, 374 (2015) 1–9.

[19] O.R. Lokare, S. Tavakkoli, V. Khanna, R.D. Vidic, Importance of feed recirculation for the overall energy consumption in membrane distillation systems, Desalination, 428 (2018) 250–254.

[20] H. Geng, J. Wang, C. Zhang, P. Li, H. Chang, High water recovery of RO brine using multi-stage air gap membrane distillation, Desalination, 355 (2015) 178–185.

[21] F. Banat, N. Jwaied, M. Rommel, J. Koschikowski, M. Wieghaus, Desalination by a "compact SMADES" autonomous solarpowered membrane distillation unit, Desalination, 217 (2007) 29–37.

[22] T.-C. Chen, C.-D. Ho, Immediate assisted solar direct contact membrane distillation in saline water desalination, J. Membr. Sci., 358 (2010) 122–130.

[23] J.H. Lienhard, M.A. Antar, A. Bilton, J. Blanco, G. Zaragoza, Solar Desalination, Annu. Rev. Heat Transfer, 15 (2012) 277–347.

[24] K. Charfi, M. Khayet, M.J. Safi, Numerical simulation and experimental studies on heat and mass transfer using sweeping gas membrane distillation, Desalination, 259 (2010) 84–96.

[25] F. Eleiwi, N. Ghaffour, A.S. Alsaadi, L. Francis, T.M. Laleg-Kirati, Dynamic modeling and experimental validation for direct contact membrane distillation (DCMD) process, Desalination, 384 (2016) 1–11.

[26] A.S. Hassan, H.E.S. Fath, M. Darwish, H. Abdulrahim, Dynamic performance of vacuum membrane distillation system, Desal. Water Treat., 57 (2016) 23196–23205.

[27] A.M. Karam, A.S. Alsaadi, N. Ghaffour, T.M. Laleg-Kirati, Analysis of direct contact membrane distillation based on a lumped-parameter dynamic predictive model, Desalination, 402 (2017) 50–61.

[28] E. Ali, J. Orfi, A. Najib, Developing and validating a dynamic model of water production by direct-contact membrane distillation, PLoS one, 15 (2020) e0230207, doi: 10.1371/journal.pone.0230207.

[29] E.M. Ali, J. Saleh, J. Orfi, A. Najib, Developing and validating linear dynamic models for direct contact membrane distillation during start-up over wide operating conditions, Comput. Chem. Eng., 134 (2020) 106678, doi: 10.1016/j.compchemeng.2019.106678.

[30] J.S. Kim, J. Chen, H.E. Garcia, Modeling, control, and dynamic performance analysis of a reverse osmosis desalination plant integrated within hybrid energy systems, Energy, 112 (2016) 52–66.

[31] N. Al-Bastaki, A. Abbas, Use of fluid instabilities to enhance membrane performance: a review, Desalination, 136 (2001) 255–262.

[32] W. Lai, Q. Ma, H. Lu, S. Weng, J. Fan, H. Fang, Effects of wind intermittence and fluctuation on reverse osmosis desalination process and solution strategies, Desalination, 395 (2016) 17–27.

[33] B.S. Richards, G.L. Park, T. Pietzsch, A.I. Schäfer, Renewable energy powered membrane technology: brackish water desalination system operated using real wind fluctuations and energy buffering, J. Membr. Sci., 468 (2014) 224–232.

[34] R.D. Gustafson, S.R. Hiibel, A.E. Childress, Membrane distillation driven by intermittent and variable-temperature waste heat: system arrangements for water production and heat storage, Desalination, 448 (2018) 49–59.

[35] L. Martínez-Díez, M.I. Vazquez-Gonzalez, Temperature and concentration polarization in membrane distillation of aqueous salt solutions, J. Membr. Sci., 156 (1999) 265–273.

[36] L. Martínez-Díez, M. Vázquez-González, F. Florido-Díaz, Study of membrane distillation using channel spacers, J. Membr. Sci., 144 (1998) 45–56.

[37] M.M. Teoh, S. Bonyadi, T.-S. Chung, Investigation of different hollow fiber module designs for flux enhancement in the membrane distillation process, J. Membr. Sci., 311 (2008) 371–379.

[38] E.M. Ali, J. Orfi, A. Najib, Nonlinear dynamic modeling and validation of a direct contact membrane distillation for water desalination, Appl. Therm. Eng., 179 (2020) 115719, doi: 10.1016/j.applthermaleng.2020.115719.

[39] E. Ali, J. Orfi, A. Najib, O. Hamdaoui, Understanding the dynamic behavior and the effect of feeding policies of a direct contact membrane distillation for water desalination, Chem. Eng. Commun., 208 (2021) 1737–1756.

[40] G. Naidu, S. Jeong, S. Vigneswaran, Influence of feed/permeate velocity on scaling development in a direct contact membrane distillation, Sep. Purif. Technol., 125 (2014) 291–300.

[41] S. George, Chemical Process Control: An Introduction to Theory and Practice, PTR Prentice Hall, Inc., NJ, USA, 1984.

Appendix-A

The separation of water by DCMD is governed by the simultaneous mass and heat-transfer mechanisms. In this section, we highlight the algorithm for solving the mass and heat transport equations to determine h_v, h_m, T_{h_m} and T_{c_m}. The latter variables are required to solve the dynamic model. The following algorithm was developed, adopting our previous experience with modeling the MD process [39,41,A1,A2]. The following algorithm assumed the process, under steady state conditions:

(1) employing the existing bulk temperatures (T_{h_b}, T_{c_b}) for the hot and cold channels, the heat-transfer coefficients of the film (h_f, h_p) could be estimated by the Nusselt number, as follows [3]:

$$\mathrm{Nu} = 0.298\mathrm{Re}^{0.646}\mathrm{Pr}^{0.316} \tag{A1}$$

where Re is Reynolds number and Pr is the Prandtl number.

(2) $T^0_{h_m} = T_{h_b}$ and $T^0_{c_m} = T_{c_b}$ were set.

(3) The vapor pressure, at the membrane interface, was calculated by the following [4]:

$$P_1 = \exp\left(23.238 - \frac{3{,}841}{T_{h_m} - 45}\right)\left(1 - C_s\right)\left(1 - 0.5C_s - 10C_s^2\right) \tag{A2}$$

$$P_2 = \exp\left(23.238 - \frac{3{,}841}{T_{c_m} - 45}\right) \tag{A3}$$

(4) The membrane coefficient, C_m, can be computed based on the active mechanism by the membrane properties and the average membrane temperature, that is, $T = \frac{T_{h_m} + T_{c_m}}{2}$. The active mechanism was determined under the following conditions [11]:

- the Knudsen flow mechanism, $k_n > 1$:

$$C_m^k = \frac{2\varepsilon r}{3\tau\delta}\left(\frac{8M_w}{\pi RT}\right)^{1/2} \tag{A4}$$

- Molecular diffusion mechanism, $k_n < 0.01$:

$$C_m^D = \frac{\varepsilon}{\tau\delta}\frac{PD}{P_a}\frac{M_w}{RT} \tag{A5}$$

- Knudsen–molecular diffusion transition mechanism, $0.01 < k_n < 1$:

$$C_m^C = \left[\frac{3}{2}\frac{\tau\delta}{\varepsilon r}\left(\frac{\pi RT}{8M_w}\right)^{1/2} + \frac{\tau\delta}{\varepsilon}\frac{P_a}{PD}\frac{RT}{M_w}\right]^{-1} \tag{A6}$$

where the Knudsen number, defined as $k_n = \lambda/d$, and where λ is the mean free path of water molecules, further expressed as Eq. (A7) [3]:

$$\lambda = \frac{k_B T}{\sqrt{2}\pi P d_e^{\,2}} \tag{A7}$$

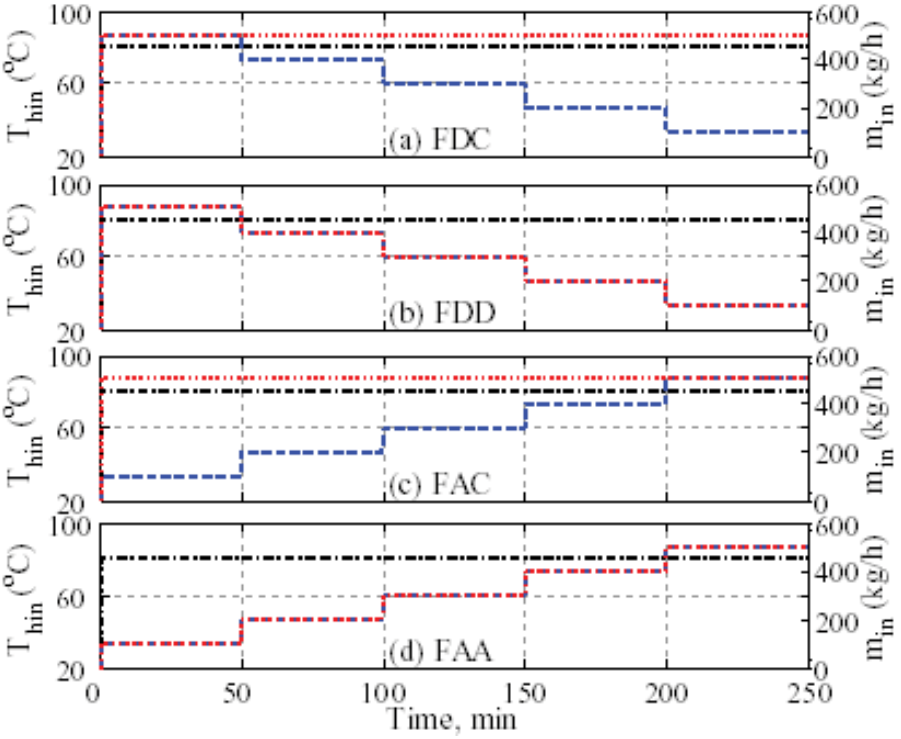

Fig. S1. Forced input profile for the process inputs: $T_{h_{in}}$ dash–and–dot line, $m_{h_{in}}$: dashed line, $m_{c_{in}}$: dotted line.

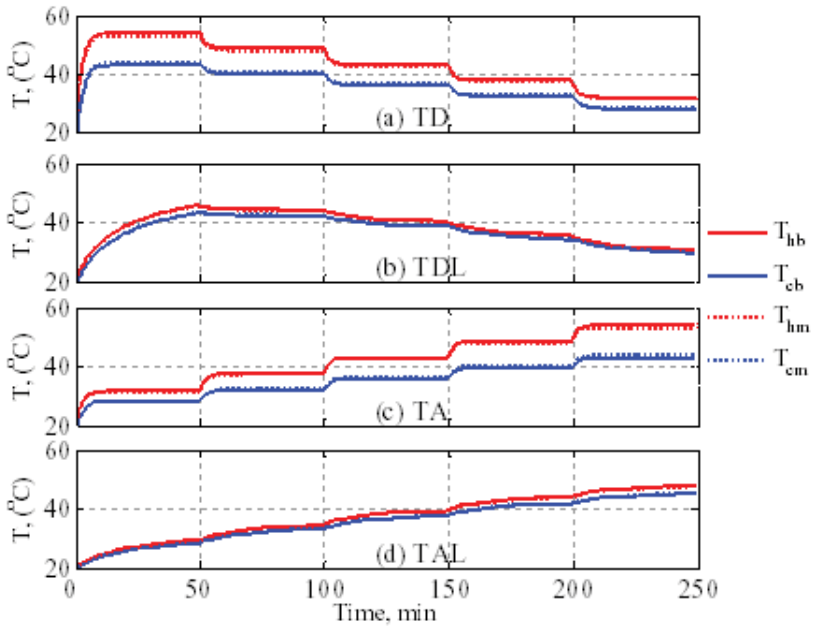

Fig. S2. Bulk-temperature response to a sequence of step changes in the hot inlet temperature: (a and b) descending and (c and d) ascending.

where T and P are the average temperature and pressure, at the membrane interface, respectively, $k_B = 1.380622 \times 10^{-23}$ and $d_e = 9.29 \times 10^{-20}$.

(5) The latent heat of vaporization, at the average membrane temperature, was calculated by the following Eq. (A3):

$$h_v(T) = 1{,}850.7 + 2.8273T - 1.6 \times 10^{-3} T^2 \quad \text{(A8)}$$

(6) The mass flux was computed by the following equation:

$$j_w = C_m(P_1 - P_2) \quad \text{(A9)}$$

(7) The overall heat-transfer coefficient was calculated, as follows [11]:

$$U = \left[\frac{1}{h_f} + \frac{1}{h_m + \dfrac{J_w h_v}{T_{h_m} - T_{c_m}}} + \frac{1}{h_p} \right]^{-1} \quad \text{(A10)}$$

where h_m is the heat-transfer coefficient of the membrane, which involves the conduction resistance. It is computed, as follows [15]:

$$h_m = \frac{k_m}{\delta} = \frac{(1-\varepsilon)k_s + \varepsilon k_g}{\delta} \quad \text{(A11)}$$

(8) At a steady state, the different heat-transfer mechanisms become equal. These equalities translate into the following expressions [11]:

$$U(T_{h_b} - T_{c_b}) = h_f(T_{h_b} - T_{h_m}) = j_w h_v + h_m(T_{h_m} - T_{c_m}) \quad \text{(A12)}$$

$$U(T_{h_b} - T_{c_b}) = h_p(T_{c_m} - T_{c_b}) = j_w h_v + h_m(T_{h_m} - T_{c_m}) \quad \text{(A13)}$$

The above equalities can be solved to calculate the new quantities of T_{h_m} and T_{c_m}:

(9) If $T_{h_m} = T^0_{h_m}$ and $T_{c_m} = T^0_{c_m}$, the iteration should be stopped. If not, set $T^0_{h_m} = T_{h_m}$ and $T^0_{c_m} = T_{c_m}$ and go back to step 3.

The above algorithm is terminated with a termination tolerance of 1×10^{-7}.

References

[A1] A. Najib, J. Orfi, E. Ali, A. Ajbar, M. Boumaaza, K. Alhumaizi, Performance analysis of cascaded membrane distillation arrangements for desalination of brackish water, Desal. Water Treat., 76 (2017) 19–29.

[A2] J. Orfi, A. Najib, E. Ali, A. Ajbar, M. AlMatrafi, M. Boumaaza, K. Alhumaizi, Membrane distillation and reverse osmosis-based desalination driven by geothermal energy sources, Desal. Water Treat., 76 (2017) 40–52.

[A3] A.K. Fard, Y.M. Manawi, T. Rhadfi, K.A. Mahmoud, M. Khraisheh, F. Benyahia, Synoptic analysis of direct contact membrane distillation performance in Qatar: a case study, Desalination, 360 (2015) 97–107.